ARTICLES
https://doi.org/10.1038/s41560-019-0387-1

nature energy

Building ultraconformal protective layers on both secondary and primary particles of layered lithium transition metal oxide cathodes

Gui-Liang Xu[1,11], Qiang Liu[2,3,11], Kenneth K. S. Lau[4], Yuzi Liu[5], Xiang Liu[1,6], Han Gao[1], Xinwei Zhou[5,7], Minghao Zhuang[1,2], Yang Ren[8], Jiadong Li[2], Minhua Shao[2], Minggao Ouyang[6], Feng Pan[9], Zonghai Chen[1], Khalil Amine[1,10]* and Guohua Chen[3]*

Despite their relatively high capacity, layered lithium transition metal oxides suffer from crystal and interfacial structural instability under aggressive electrochemical and thermal driving forces, leading to rapid performance degradation and severe safety concerns. Here we report a transformative approach using an oxidative chemical vapour deposition technique to build a protective conductive polymer (poly(3,4-ethylenedioxythiophene)) skin on layered oxide cathode materials. The ultraconformal poly(3,4-ethylenedioxythiophene) skin facilitates the transport of lithium ions and electrons, significantly suppresses the undesired layered to spinel/rock-salt phase transformation and the associated oxygen loss, mitigates intergranular and intragranular mechanical cracking, and effectively stabilizes the cathode–electrolyte interface. This approach remarkably enhances the capacity and thermal stability under high-voltage operation. Building a protective skin at both secondary and primary particle levels of layered oxides offers a promising design strategy for Ni-rich cathodes towards high-energy, long-life and safe lithium-ion batteries.

Layered lithium transition metal oxides ($LiNi_xCo_yMn_{1-x-y}O_2$, hereafter referred to as NCM) have been considered as the most promising cathode materials for next-generation lithium-ion batteries[1]. In the past few decades, with significant advances of in-depth understanding of the failure mechanism[2–4] and rational engineering of bulk/surface structure[5–8], the electrochemical performance of layered oxides has been significantly improved. Pushing NCM cathode materials towards high-voltage operation is an effective way to further increase the energy density of batteries[9]. However, extraction of lithium ions from the host structure of layered oxide cathode materials during high-voltage and/or high-temperature cycling would initiate a layered to spinel/rock-salt phase transformation because of the intensified migration of transition metal cations into the lithium layer (that is, cation mixing)[10,11], which will lead to structural instability and further capacity/voltage fade.

To increase the packing density, most of the reported layered cathodes are composed of microsized secondary particles, which are formed by densely packed nanosized primary particles[1,5]. This approach brings high tap density, but introduces some drawbacks such as intergranular cracking during electrochemical cycling[12,13]. Furthermore, Yan et al. observed the nucleation and growth of intragranular cracks in a commercial $LiNi_{1/3}Co_{1/3}Mn_{1/3}O_2$ (NCM111) cathode[14]. Such intragranular cracks are caused by the dislocation activity within the primary particles, which is markedly aggravated during high-voltage operation. These intergranular and intragranular microcracks not only induce mechanical stress inside the secondary particles, but also can act as reaction sites with the electrolytes, leading to the generation of a thick solid–electrolyte interphase layer along the active surface of the primary particles and further inhibiting the transport of electrons and lithium ions[15]. In addition, corrosion and dissolution of transition metal cations in the electrolytes also result in performance degradation of NCM cathode materials[16].

Surface modification on secondary particles is a widely deployed strategy to mitigate cathode reactivity[17]. However, the microstructural evolution caused by the reaction between the primary particles and the electrolyte would still lead to structural degradation during cycling[18]. Thus, much research has been devoted to surface engineering at the primary particle level. Atomic layer deposition can coat primary particles with oxides or solid electrolytes with precise ångström-level thickness and uniformity[19]. However, oxide-coated materials usually suffer from decreased electronic and ionic conductivity, resulting in limited improvements in the cell electrochemical performance[20]. Moreover, the surface structures of oxide-coated cathodes would be under continuous damage by localized high-concentration acidic species because of the low tolerance of oxides to HF, which would weaken the protection of cathode materials over extended periods of cycling or ageing[21]. Solid electrolyte coating is another promising way to address the long-standing capacity and voltage fade of layered cathodes[20,22–24]. Yan et al. reported a Li_3PO_4-infused Ni-rich $LiNi_{0.76}Co_{0.10}Mn_{0.14}O_2$ cathode by further melting the as-coated Li_3PO_4 layer to seal the grain boundaries between individual

[1]Chemical Sciences and Engineering Division, Argonne National Laboratory, Lemont, IL, USA. [2]Department of Chemical and Biological Engineering, The Hong Kong University of Science and Technology, Kowloon, Hong Kong, China. [3]Department of Mechanical Engineering, The Hong Kong Polytechnic University, Kowloon, Hong Kong, China. [4]Department of Chemical and Biological Engineering, Drexel University, Philadelphia, PA, USA. [5]Centre for Nanoscale Materials, Argonne National Laboratory, Lemont, IL, USA. [6]State Key Laboratory of Automotive Safety and Energy, Tsinghua University, Beijing, China. [7]Department of Mechanical and Energy Engineering, Indiana University–Purdue University Indianapolis, Indianapolis, IN, USA. [8]X-ray Science Division, Argonne National Laboratory, Lemont, IL, USA. [9]School of Advanced Materials, Peking University, Shenzhen Graduate School, Shenzhen, China. [10]Materials Science and Engineering, Stanford University, Stanford, CA, USA. [11]These authors contributed equally: G.-L. Xu, Q. Liu. *e-mail: amine@anl.gov; Guohua.chen@polyu.edu.hk

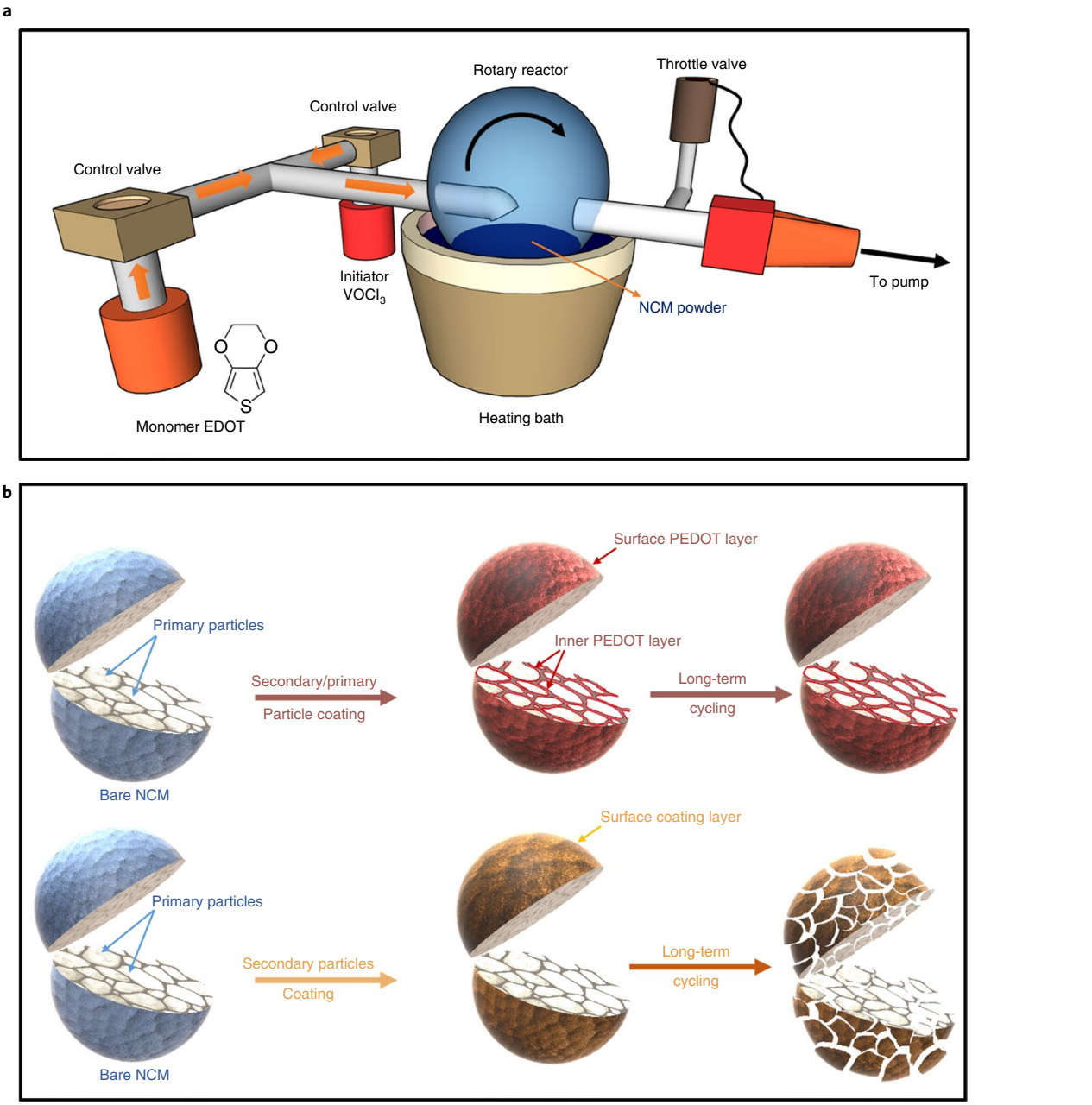

Fig. 1 | The oCVD process and particle structural differences between different coatings. a, A schematic diagram of the experimental oCVD setup. The oCVD process relies on uniform vapour (oxidant and monomer) adsorption and subsequent in situ polymerization on the NCM particle (secondary/primary) surface. **b**, An illustration of the structural stability of both secondary/primary particle coating and secondary particle coating only after long-term cycling. The oCVD process led to conformal PEDOT coating on both secondary and primary particles, resulting in no particle cracking after a long cycle life, while secondary particle coating only by conventional processes resulted in particle cracking after a long cycle life.

primary particles[24]. Their modified cathode shows about 10% cycle stability improvement over 200 cycles, although rate capability was lower in comparison with the bare cathode material, which may be attributable to the limited electronic conductivity of phosphates. Thus, a rational surface structure engineering that can resolve all of the aforementioned crystal/interfacial problems without sacrificing the transport of electrons and lithium ions during charge–discharge is highly desirable.

Herein, we present an approach by building a protective conductive polymer skin on various types of layered cathode, including commercial NCM111 (the most common NCM cathode), a representative Ni-rich cathode ($LiNi_{0.85}Co_{0.1}Mn_{0.05}O_2$) and a high-energy Li-rich ($Li_{1.2}Mn_{0.54}Ni_{0.13}Co_{0.13}O_2$) cathode. Using an oxidative chemical vapour deposition (oCVD) technique, an ultraconformal, highly electronically conductive and ionically permeable poly(3,4-ethylenedioxythiophene) (PEDOT) skin was successfully built on both secondary and primary particles of layered oxide cathode materials. This approach resulted in significantly enhanced capacity retention and thermal stability. Combining multiple characterization techniques, we found that building ultraconformal protective layers on both secondary and primary particles of layered oxides can enhance the structural (phase and morphology) stability, and also stabilize the cathode–electrolyte interface. This study offers a strategy to mitigate the electrochemical, mechanical and thermal as well as their

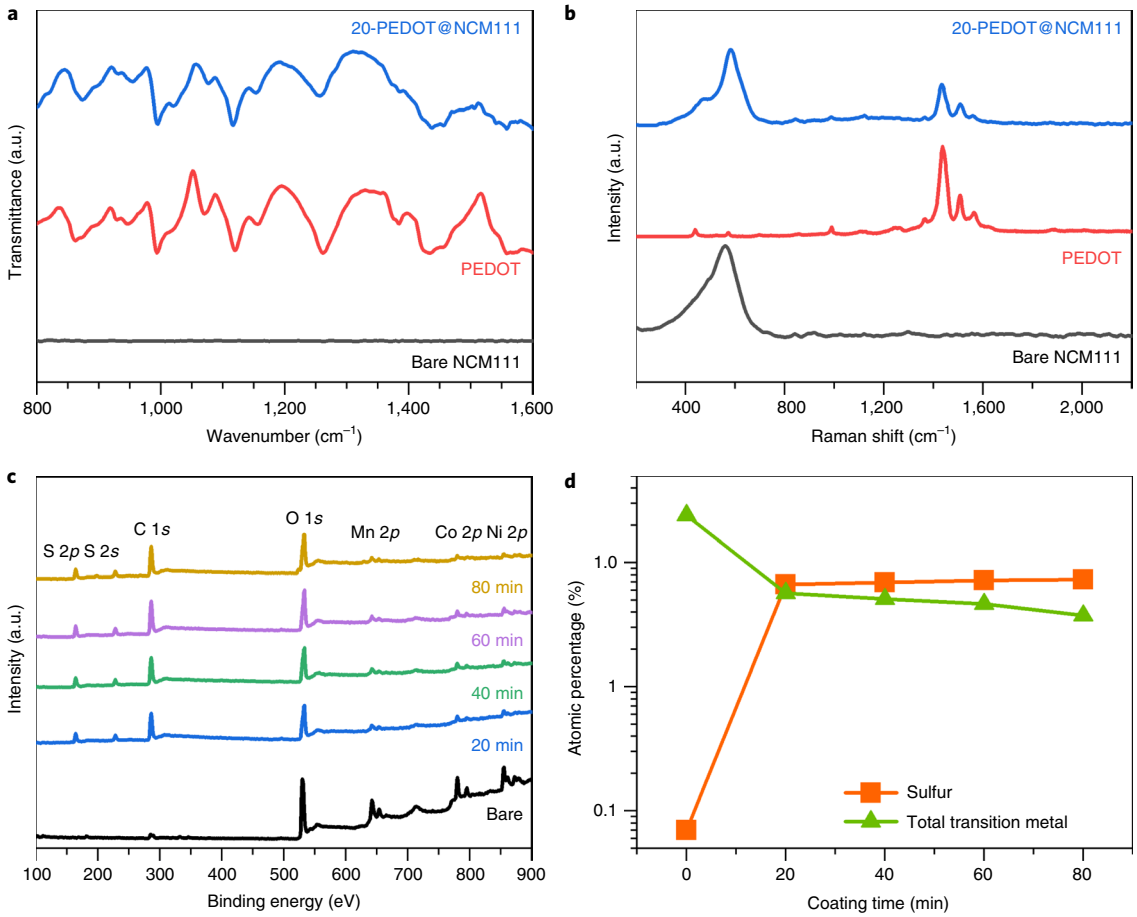

Fig. 2 | Surface characterization confirming the formation of PEDOT skin. a,**b**, Fourier-transform infrared (**a**) and Raman (**b**) spectra of bare NCM111, 20-PEDOT@NCM111 and PEDOT. **c**, X-ray photoelectron spectra of the bare and PEDOT-skinned NCM111 at various oCVD times. **d**, Atomic percentages of the transition metal (M = Ni, Co and Mn) and sulfur as a function of oCVD time.

coupling effects on the performance degradation of layered lithium metal oxide cathodes under aggressive conditions.

Building PEDOT skin on layered cathodes using oCVD

The NCM111 cathode used in this work exhibits typical microsized spherical secondary particles and a layered structure with a space group of *R*-3*m* (Supplementary Fig. 1a,b). Building a PEDOT skin on both secondary and primary particles of the NCM111 cathode was carried out using an oCVD technique. oCVD was first reported to fabricate a PEDOT coating on nanofibres to enhance efficiency in organic electronic devices[25]. In this solvent-free process, the step-growth polymerization relies on the simultaneous introduction of a volatile oxidant and monomer[26]. We used an oxidant, $VOCl_3$, to enable an ultraconformal PEDOT skin formation (see Supplementary Fig. 2 for the effect of the oxidant on the skin conformality and cycle stability).

During the oCVD process, as shown in Fig. 1a, the 3,4-ethylenedioxythiophene (EDOT) monomer and $VOCl_3$ oxidant vapours were simultaneously introduced into a rotary reactor, and then adsorbed onto the NCM111 particle surface. Thereafter, the film polymerized spontaneously, following an oxidative polymerization path, into a conformal macromolecular PEDOT skin on each primary particle. In addition, conductive polymers such as PEDOT are highly electronically conductive and ionically permeable (see Supplementary Fig. 3) and could be used as a mixed ion–electron conductor for power electronics[27]. Hence, such surface structure engineering by building an ultraconformal protective skin on NCM cathodes at both secondary and primary particle levels (Fig. 1b) could significantly enhance their crystal and interfacial structural stability without affecting the transport of lithium ions and electrons. In contrast, surface coating only on the secondary particles cannot protect the primary particles, in which the electrolyte can still penetrate along the grain boundaries and thus cause structural degradation and further capacity and voltage decay over long-term cycling. By controlling the oCVD time, we have prepared NCM111 cathodes with different thicknesses of PEDOT skin (*x*-PEDOT@NCM111, where *x* refers to the deposition time in minutes) to systematically investigate the effect of skin thickness on the cycle performance and unravel the governing kinetics and mechanisms behind the enhanced performance.

Characterization of cathode materials

To confirm the chemical composition of the PEDOT skin, we carried out surface characterization using Fourier-transform infrared spectroscopy, Raman spectroscopy and X-ray photoelectron spectroscopy. The peaks of the 20-PEDOT@NCM111 in both Fourier-transform infrared (Fig. 2a) and Raman spectra (Fig. 2b) match reasonably well with those of the as-prepared PEDOT, indicating that the skin obtained is PEDOT. In addition, the full X-ray photoelectron spectra in Fig. 2c present the appearance of PEDOT characteristic elements (sulfur and carbon) after the oCVD process, strongly confirming the presence of PEDOT. Notably, the intensities of the S 2*p*, S 2*s* and C 1*s* peaks are strengthened while those of the Mn 2*p*, Co 2*p* and Ni 2*p* (from bulk NCM111) are weakened as the

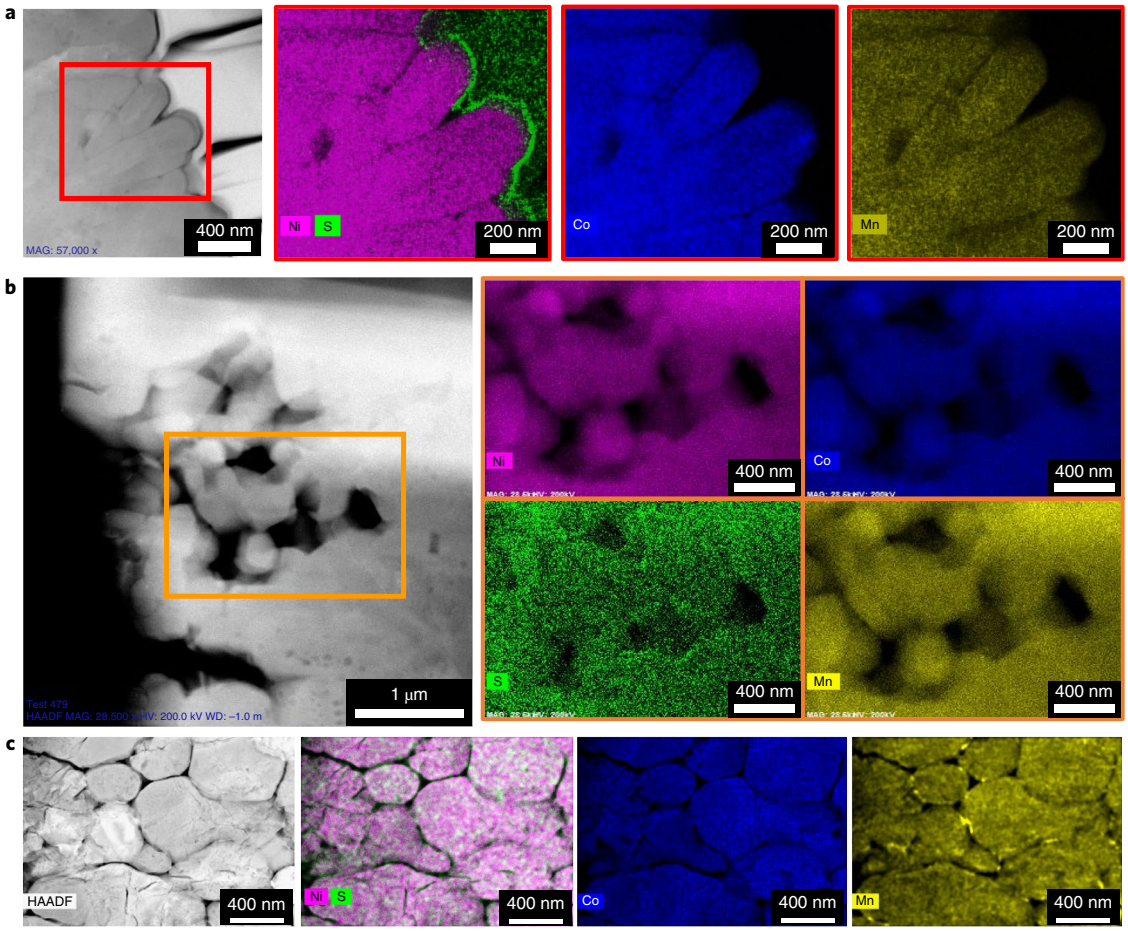

Fig. 3 | TEM results confirming PEDOT coating on secondary/primary particles of NCM cathodes. a, A STEM-HAADF image of the surface secondary particles of 60-PEDOT@NCM111, and the corresponding EDS element mapping of S, Ni, Co and Mn taken from the selected section. **b**, A STEM-HAADF image of the inner primary particles of 60-PEDOT@NCM111, and the corresponding EDS element mapping of S, Ni, Co and Mn taken from the selected section. **c**, A STEM-HAADF image and EDS mapping of the inner primary particles in the 60-PEDOT@Ni-rich ($LiNi_{0.85}Co_{0.1}Mn_{0.05}O_2$) cathode.

oCVD time is increased. When the atomic percentages of transition metals (Ni, Co and Mn) and S (signature element of PEDOT) are plotted as a function of oCVD time (Fig. 2d), the trend is more evident. This trend can be interpreted as the PEDOT skin thickness increasing with oCVD time. With all of the characterization results, one can conclude that the PEDOT skin has been successfully built on the NCM111 cathode particles using the oCVD technique.

The morphology features of *x*-PEDOT@NCM111 samples can be seen from the transmission electron microscopy (TEM) images. As evident from the images (Supplementary Fig. 4a), the PEDOT skin covers the NCM111 particles completely, homogeneously and conformably with no interfacial contact gaps. Another advantage of oCVD is that the thickness can be precisely controlled by varying the oCVD time. As displayed in the high-resolution TEM images (Supplementary Fig. 4b), the thickness increased from 7 to 14, 20 and 28 nm with 20, 40, 60 and 80 min of oCVD, respectively. Interestingly, the thickness and the loading of PEDOT are directly proportional to the oCVD time (see Supplementary Fig. 5 and the PEDOT skin loading determined by thermo-gravimetric analysis in Supplementary Fig. 6), suggesting that the skin thickness can be engineered as desired.

To confirm the capability of oCVD in building PEDOT skin at both primary and secondary particle levels, specimens were prepared and observed by scanning transmission electron microscopy-high-angle annular dark-field imaging (STEM-HAADF) as described in Methods. As clearly shown in Fig. 3a, PEDOT can act as a coating layer to homogeneously cover the surface of secondary particles. The STEM-HAADF micrograph of the 60-PEDOT@NCM111 shown in Fig. 3b further illustrates the interior structure, with many microvoids seen between individual primary particles. These voids originate from the pristine NCM111 cathode material, and are caused by the evolution of H_2O and CO_2 during the synthesis process of layered NCM cathode materials[5,28]. The oCVD technique used in this case has also led to a uniform and thin PEDOT skin on primary particles. Energy-dispersive X-ray spectrometry (EDS) element mapping (Fig. 3b) of a randomly selected area revealed the homogeneous distribution of S, confirming the successful formation of PEDOT skin on the inner primary particles.

To confirm the effectiveness of oCVD coating on other types of cathode material, we have further applied this approach on a densely packed Ni-rich ($LiNi_{0.85}Co_{0.1}Mn_{0.05}O_2$) cathode with a tap density of 2.5 g cm^{-3} and a Li-rich $Li_{1.2}Mn_{0.54}Ni_{0.13}Co_{0.13}O_2$ cathode. The results show that PEDOT is still able to fill the grain boundaries formed by the primary particles (Fig. 3c) and form a conformal layer on the particle surface (Supplementary Fig. 7).

Figure 4a,b shows two-dimensional contour plots for the structural evolution of bare NCM111 and 60-PEDOT@NCM111 cathodes during the first charge–discharge cycle at *C*/10. The Bragg reflections in Fig. 4a,b indicate that both samples have a layered α-$NaFeO_2$ structure before charge–discharge cycling. Comparison with the whole set of in situ high-energy X-ray diffraction (HEXRD) patterns reveals that their structural evolutions during charge–discharge are quite different.

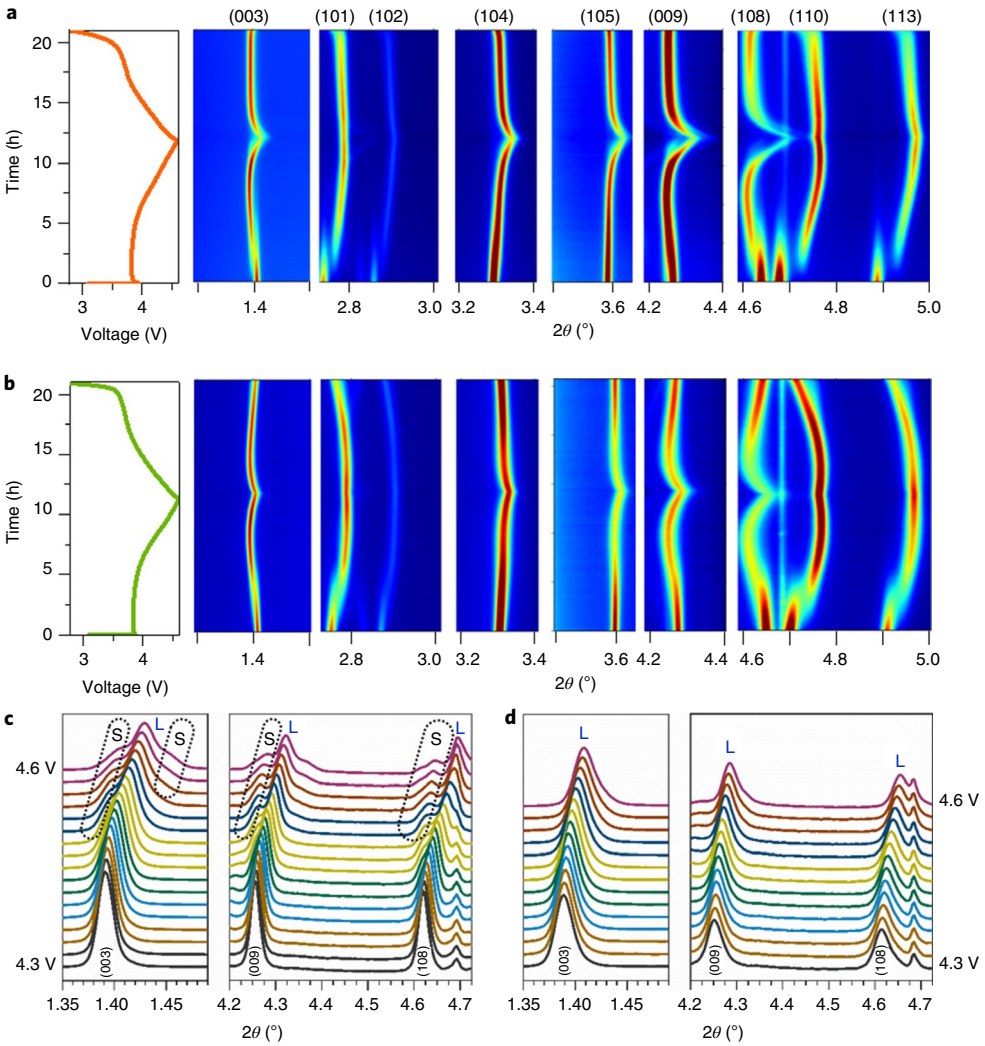

Fig. 4 | In situ synchrotron HEXRD characterization of bare NCM111 and 60-PEDOT@NCM111 cathodes during charge–discharge. a,**b**, Voltage profiles and the corresponding two-dimensional contours plot of the HEXRD pattern evolution of bare NCM111 (**a**) and 60-PEDOT@NCM111 (**b**) cathodes during the initial charge–discharge process at *C*/10. **c**,**d**, Selected in situ HEXRD patterns of bare NCM111 (**c**) and 60-PEDOT@NCM111 (**d**) cathodes in the high-voltage (4.3–4.6 V) region during charge at *C*/10. L and S in **c** and **d** represent layered and spinel-like structures, respectively.

The 60-PEDOT@NCM111 cathode has a more symmetric structural evolution during the first cycle, in which most of the diffraction peaks return to their original 2θ positions after discharge (Fig. 4b, Supplementary Fig. 8). This finding indicates a highly reversible delithiation–lithiation process. In contrast, for the bare NCM111 cathode, many peaks have deviated from their original 2θ positions after the first cycle, as indicated by the (003), (101), (102), (108), (110) and (113) peaks (Fig. 4a, Supplementary Fig. 9). On long-term cycling, such variations would adversely accumulate, leading to structural degradation and further capacity and voltage decay. The HEXRD pattern of bare NCM111 after 200 charge–discharge cycles showed that the layered structure has obviously been deteriorated (Supplementary Fig. 10).

The PEDOT skin coating can also suppress the undesired layered to spinel/rock-salt structural evolution during high-voltage charge. At the end of the first charge, for the bare NCM111 cathode, the appearance of a second phase is indicated by the weak shoulder peaks marked by dark dotted lines in Fig. 4c. These peaks correspond to the formation of surface phases, such as defect spinel-like structures with the *Fd*-3*m* space group[29], which is usually associated with oxygen loss. Such oxygen evolution and the crystal structure mismatch between the layered structure and spinel/rock-salt phase would lead to severe microstrain (associated with peak broadening) within a primary particle, which would deteriorate both surface and bulk structural stability. In the case of 60-PEDOT@NCM111, the aforementioned peaks are not seen (Fig. 4d), indicating that the layered structure is well preserved even in the highly charged state. All of these features are identical in the subsequent charge–discharge cycle (Supplementary Fig. 11), further confirming the effectiveness of the PEDOT skin in stabilizing the crystal structures during repeated extraction and insertion of lithium ions.

The cell volume change during charge–discharge is also mitigated by the PEDOT skin coating. Compared with the bare NCM111 cathode, the 60-PEDOT@NCM111 cathode showed 50% decrease in terms of volume changes during charging (Supplementary Figs. 12 and 13). Such reduction can significantly mitigate the anisotropic volume change of each primary particle and thus suppress the intergranular microcracks inside the secondary particles. Furthermore, in situ HEXRD of 60-PEDOT@NCM111 cathode at 1 *C* reveals that the layered to spinel/rock-salt phase transition is suppressed even at an elevated rate (Supplementary Fig. 14).

To reveal the function of the PEDOT skin coating, bare NCM111 and *x*-PEDOT@NCM111 cathodes were electrochemically charged–discharged in half-cells. The first three charge–discharge cycle curves

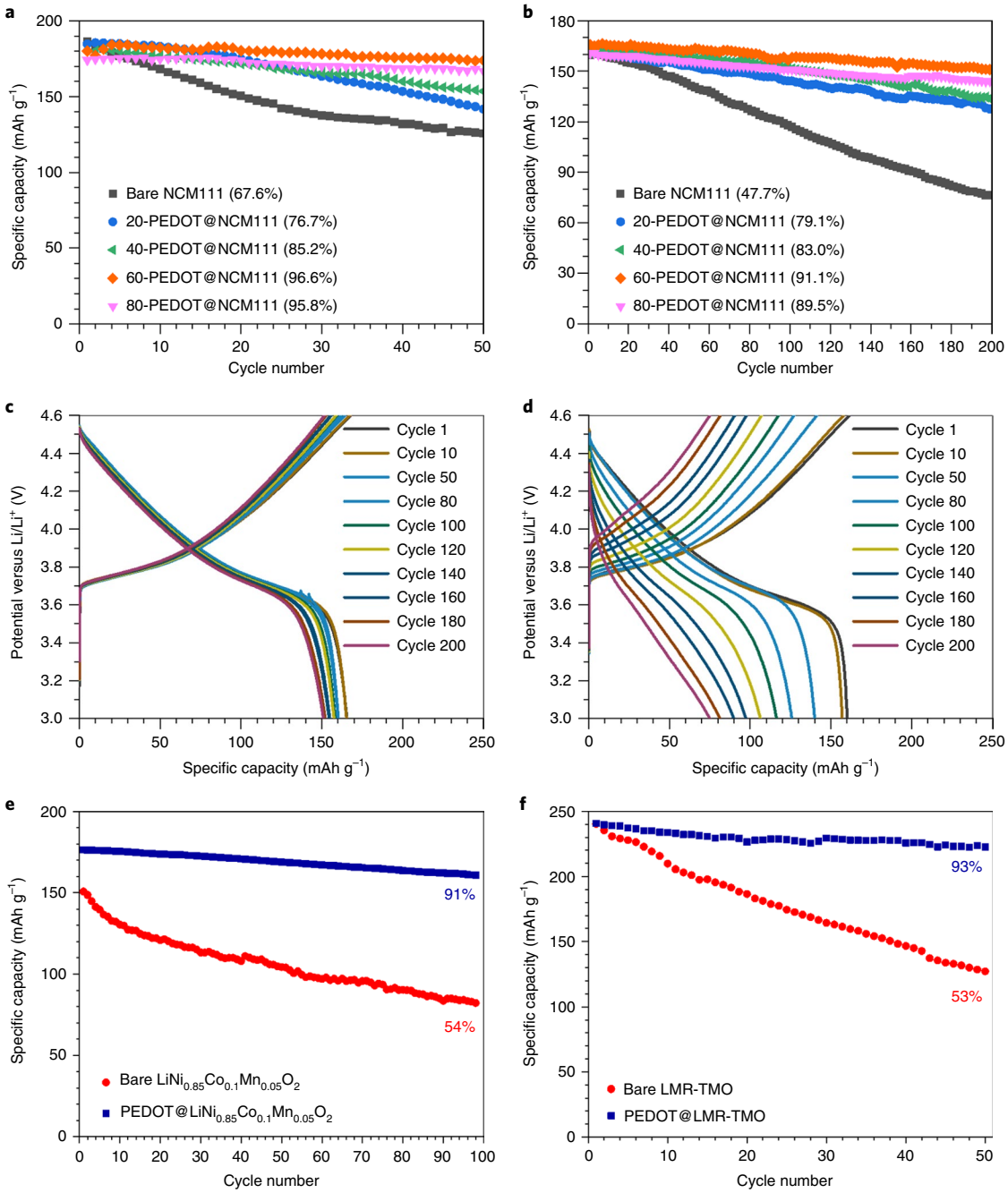

Fig. 5 | The effects of PEDOT coating on electrochemical performance. a,**b**, The capacity retention of bare and PEDOT-skinned NCM111 at *C*/10 (**a**) and 1 *C* (**b**). **c**,**d**, Half-cell voltage stability of 60-PEDOT@NCM111 (**c**) and bare NCM111 (**d**) at 1 *C*. **e**, The cycle performance of bare and optimal PEDOT-skinned Ni-rich $LiNi_{0.85}Co_{0.1}Mn_{0.05}O_2$ cathode at 1 *C* in the range of 2.7–4.3 V. **f**, The cycle performance of bare and PEDOT-skinned $Li_{1.2}Mn_{0.54}Ni_{0.13}Co_{0.13}O_2$ (LMR-TMO) cathodes at *C*/10 in the range 2.0–4.8 V. The capacities were calculated based on the total mass of PEDOT skin and layered cathodes.

at *C*/10 (Supplementary Fig. 15) show that the PEDOT skin does not fundamentally affect the specific capacity or the charge–discharge voltage profile, owing to the combined high electronic conductivity and ionic permeability of the PEDOT skin. The electrochemical test results show that the PEDOT skin substantially improves the cycling stability. As displayed in Fig. 5a, the capacity retention rate at *C*/10 over 50 cycles can be improved to 76.7, 85.2, 96.6 and 95.8% from 67.6% (for bare NCM) with 20, 40, 60 and 80 min of oCVD, respectively. At a higher rate of 1 *C*, a more remarkable cycling stability enhancement is observed in Fig. 5b, from 47.7% for bare NCM to 79.1, 83.0, 91.1 and 89.5% after 200 cycles with 20, 40, 60 and 80 min of oCVD, respectively. From the capacity retention values at both *C*/10 and 1 *C*, 60 min duration with 20 nm thickness is found to be an optimal oCVD condition for the best performance. It is especially noteworthy that the capacity retention rate of 91.1% over 200 cycles at such a high cut-off voltage (4.6 V) and high rate (1 *C*) is an impressive improvement without using electrolyte additives such as lithium bis(oxalato)borate, lithium difluoro(oxalato)borate or fluoroethylene carbonate.

In addition to the significant capacity retention improvements, as shown in the charge–discharge voltage profiles during cycling (Fig. 5c,d), the voltage decay is also markedly mitigated

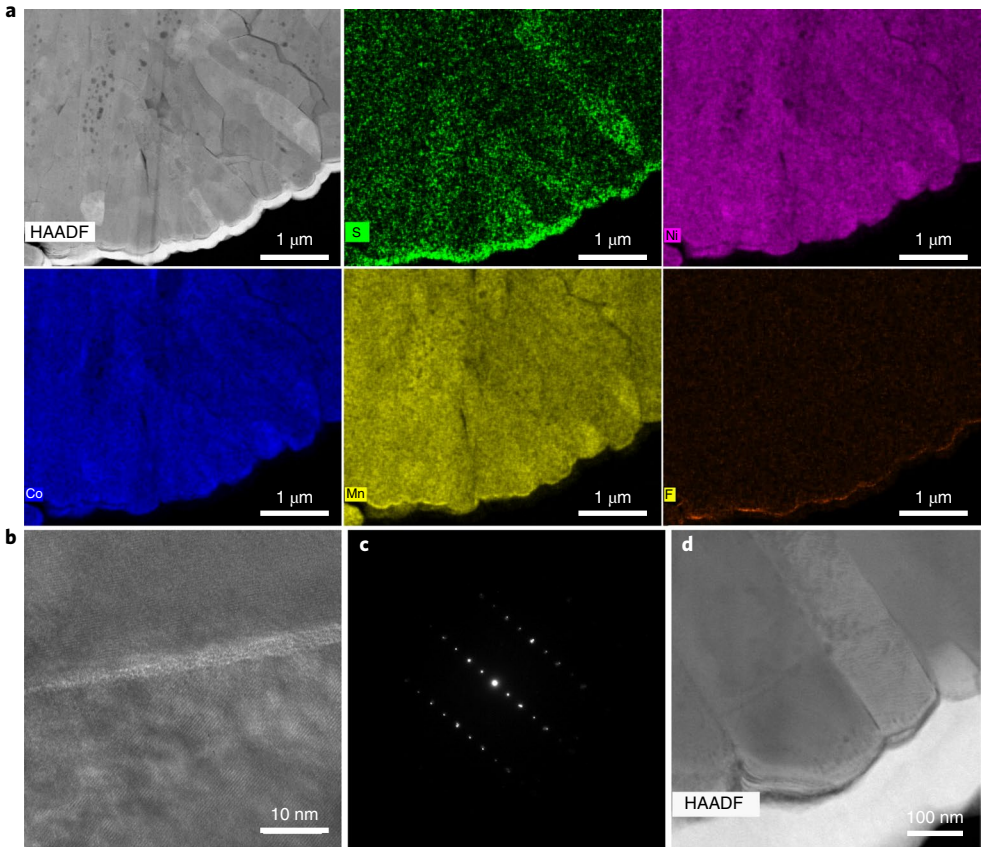

Fig. 6 | The structural stability of the 60-PEDOT@NCM111 cathode after cycling. a–d, A STEM-HAADF image and the corresponding EDS mapping (**a**), a high-resolution TEM image (**b**), a selected area electron diffraction pattern (**c**) and a STEM-HAADF image (**d**) of the 60-PEDOT@NCM111 cathode after 200 charge–discharge cycles at 1C in the range of 3.0–4.6 V.

in the case of 60-PEDOT@NCM111, indicating the suppression of the undesired structural transformation from layered to spinel/rock salt. Furthermore, the cycle stability of the layered Ni-rich $LiNi_{0.85}Mn_{0.05}Co_{0.1}O_2$ cathode and Li-rich $Li_{1.2}Mn_{0.54}Ni_{0.13}Co_{0.13}O_2$ cathode can also be significantly improved by building an ultra-conformal PEDOT skin using oCVD (Fig. 5e,f), demonstrating the broad application of this approach in the development of better materials towards high-energy and long-life rechargeable batteries. In addition, a full cell with 60-PEDOT@NCM111/graphite also exhibited good cycle stability, indicating that there is no incompatibility issue for PEDOT with anode materials (Supplementary Fig. 16).

Structural and interfacial stability after cycling

Since the PEDOT skin coating can enhance the long-term cycle stability, we further examined the 60-PEDOT@NCM111 cathode after 200 cycles by STEM-HAADF and EDS element mapping. The STEM-HAADF images in Fig. 6a and Supplementary Fig. 17 reveal that the artificial PEDOT skin is still well preserved without breaking or detaching after long-term cycling at aggressive rates and high cut-off voltage. The corresponding elemental mapping further shows the uniform distribution of S on the particle, confirming that the artificial PEDOT skin remains intact over extended cycling. Similar results can be found in the case of the PEDOT-skinned Ni-rich cathode (Supplementary Fig. 18). In addition, most of the fluorine (signature element of electrolyte) only appeared at the outer surface of the secondary particles and did not penetrate into the grain boundaries between primary particles. Therefore, one can conclude that the artificial PEDOT skin is stable and sufficiently robust to provide long-term protection of the layered NCM cathodes without potential harm to the battery system related to either coating detachment or transition metal dissolution.

Furthermore, after 200 charge–discharge cycles, the layered structure of the NCM111 cathode can still be well maintained (Fig. 6b,c). In addition, we found that bare NCM111 showed intensive intergranular cracking after 200 cycles, while these cracks did not appear in the case of the 60-PEDOT@NCM111 cathode (Supplementary Fig. 19). The artificial PEDOT skin was also found to mitigate the formation of intragranular cracking within primary particles. As shown in Fig. 6d, there is no obvious formation of intragranular cracking after 200 charge–discharge cycles. This may be because of the suppression of oxygen release from the PEDOT-skinned NCM111 cathode at high temperature due to the protection of the artificial PEDOT skin (as discussed later).

The cathode–electrolyte interface is the key area for Li^+ transport, charge transfer and parasitic reactions. Thus, the electrochemical impedance variations were monitored during cycling by electrochemical impedance spectroscopy to gain insight into the mechanism behind the cycling performance improvement. The obtained Nyquist plots consist of two semicircles followed by an inclined line in the low-frequency region, as shown in Fig. 7a,b. The semicircle in the high-frequency region is generally interpreted as the surface film resistance, while the one in the medium–low-frequency region represents the charge-transfer resistance. The two semicircles become three times larger during the initial 50 cycles for bare NCM111 (Fig. 7a), indicating a marked impedance increase on cycling. The increase is generally related to the thickening of a less conductive surface layer such as LiF, Li_2CO_3 and $LiFPO_x$ on the bare NCM111 cathode[30]. As displayed in Fig. 7b, the artificial PEDOT skin substantially suppresses the impedance increase for

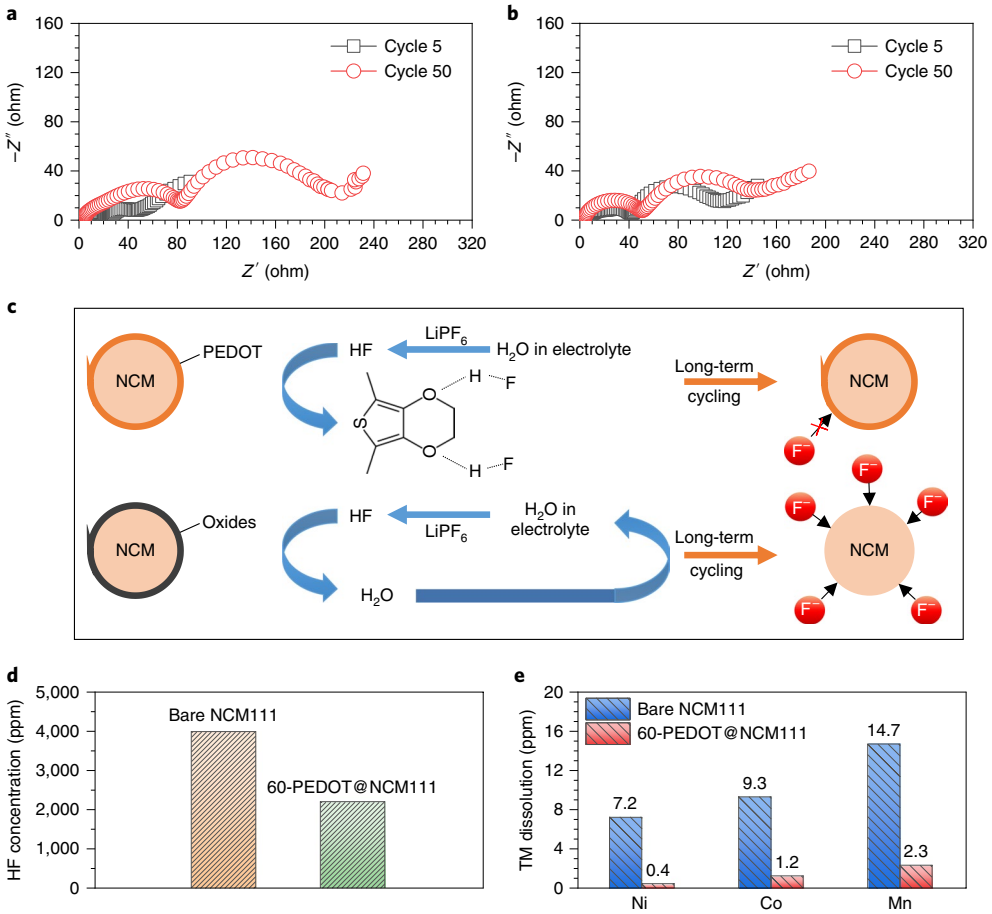

Fig. 7 | The effect of PEDOT coating on stabilizing the cathode–electrolyte interface. a,**b**, Impedance spectrum evolution of bare NCM111 (**a**) and 60-PEDOT@NCM111 (**b**) cathodes in different charge–discharge cycles. **c**, A schematic illustration of transition metal cation dissolution in PEDOT-skinned and oxide-coated NCM cathodes, in which PEDOT has an HF-scavenging effect through chemical adsorption with HF, while oxides undergo an HF generation–corrosion loop. **d**,**e**, The effect of the artificial PEDOT skin on HF scavenging (**d**) and transition metal (TM) cation dissolution (**e**) after 200 cycles.

the NCM111 cathode. This significant difference indicates that the artificial PEDOT skin improves the NCM111 cathode–electrolyte interfacial stability and maintains the ionic and electronic conductivity of the interface during cycling.

As well as from the interfacial passive layer growth, transition metal cation dissolution caused by HF attack is another common detrimental factor in capacity decay. The dissolved transition metal cations can migrate through the electrolyte to the anode, causing changes to the solid–electrolyte interphase and leading to increased impedance, decreased reversible capacity and reduced lifespan[16,31]. Previously, it was reported that PEDOT has a tendency to chemically coordinate small molecules such as HBr and H_2SO_4 (refs. [32,33]), which can significantly decrease the concentration of HF in the electrolytes and hence alleviate the transition metal cation dissolution. Actually, the dioxane ring in the molecular structure of PEDOT can serve as an HF coordination site through formation of O–H–F covalent bonds, as demonstrated in Fig. 7c. However, in the case of oxide-coated NCM cathodes, the materials undergo an HF generation–corrosion loop, which will expose them directly to the electrolyte after long-term cycling, resulting in continuous transition metal cation dissolution.

To confirm the HF-scavenging effect of the artificial PEDOT skin, PEDOT-skinned NCM111 and bare cathodes were mixed with HF-bearing electrolyte and the HF concentration was monitored after 48 h (Fig. 7d). As expected, the artificial PEDOT skin decreases the overall HF concentration by around 50%. Figure 7e further compares the transition metal cation dissolution after 200 cycle at 1 *C*. As shown, the artificial PEDOT skin significantly minimizes the dissolution of transition metal cations compared with bare material.

Thermal stability

The thermal stability and safety of cathode materials under high-voltage charging are essential concerns in evaluating the feasibility of battery materials for practical applications[34]. It has been reported that the charged NCM111 goes through a phase transition accompanied by oxygen species release on heating[35]. The oxygen species (for example O_2^-, O^-, O_2^{2-} and O_2) are highly reactive and can accelerate severe thermal runaway by reacting with flammable electrolytes. Furthermore, the internal pressure resulting from oxygen release is one of the primary driving forces for intragranular cracking within the primary particles, which could further aggravate failure in layered cathodes[36]. Therefore, the thermal stability and the oxygen (O_2, $m/z=32$) evolution behaviour of the bare and PEDOT-skinned NCM111 cathodes in the highly charged state were characterized by differential scanning calorimetry (DSC) and mass spectrometry, respectively.

Figure 8a shows the DSC curves of the highly charged bare NCM111 and 60-PEDOT@NCM111 cathodes without the presence of electrolyte. The delithiated bare NCM111 exhibits an exothermic

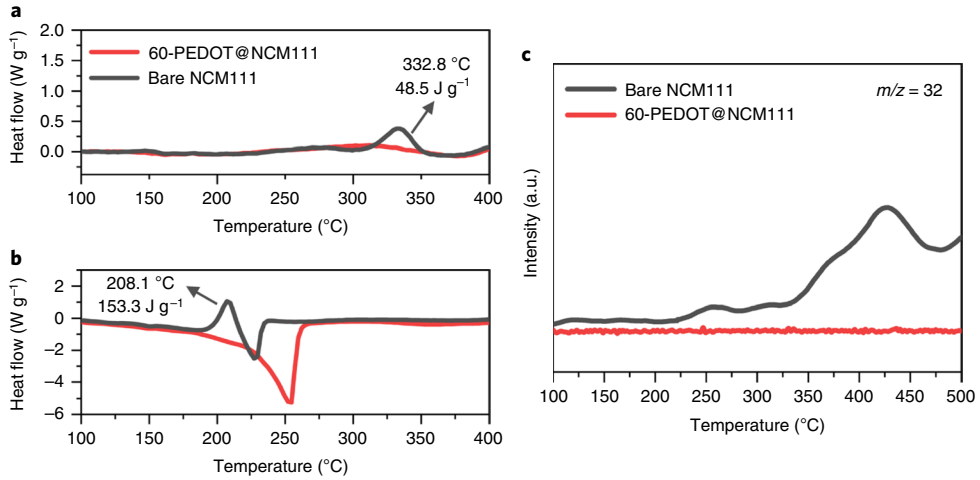

Fig. 8 | Effect of PEDOT coating on thermal stability of NCM111 cathode. a,**b**, DSC curves of delithiated bare NCM111 and 60-PEDOT@NCM111 without (**a**) and with (**b**) the presence of electrolyte. **c**, Mass spectra for O_2 evolution behaviour of delithiated bare NCM111 and 60-PEDOT@NCM111 in the presence of electrolyte during heating to 500 °C.

peak at 332.8 °C with an enthalpy change (ΔH) of 48.5 J g^{-1}. This peak corresponds to the transformation of layered structure to spinel phase[37]. For the delithiated 60-PEDOT@NCM111 cathode, the major exothermic peak related to the phase transformation was not observed, indicating that the artificial PEDOT skin can effectively suppress the undesired layered to spinel phase transition under a thermal driving force. Big changes were observed when the delithiated cathode was mixed with the electrolyte. As shown in Fig. 8b, for delithiated bare NCM111, the exothermic peak starts earlier at 208.1 °C, with ΔH rising to 153.3 J g^{-1}. This behaviour is caused by the electrolyte serving as a reduction agent that aggravates the degradation of layered structures. In the case of the 60-PEDOT@NCM111 cathode, only one endothermic peak from the decomposition of the electrolytes was observed, at around 250 °C. This indicates that the reaction between the delithiated layered cathode and electrolyte is effectively inhibited owing to the protective PEDOT skin on each individual particle. Figure 8c further shows the profiles of oxygen release for the highly charged bare NCM111 and 60-PEDOT@NCM111 cathodes in the presence of electrolytes. For the bare NCM111, there are two peaks centred at 250 and 425 °C, which correspond to the transformation of layered structure to spinel structure and then to rock-salt structure, respectively[35]. Such processes are usually associated with irreversible oxygen loss, which would induce a severe safety concern. Fortunately, there is no evolution of oxygen after building the artificial PEDOT skin, indicating that the layered to spinel/rock-salt phase transformation is effectively inhibited even at high temperatures. This can further alleviate the chemical crosstalk of oxygen from cathode to anode as reported previously[38]. Hence, building an artificial PEDOT skin at both secondary and primary particle levels for NCM cathodes would remarkably improve the safety performance of lithium-ion batteries.

Conclusions

In summary, we have demonstrated a strategy to significantly improve the electrochemical and thermal stability of layered oxide cathode materials by building an ultraconformal conductive polymer skin at both secondary and primary particle levels. This surface engineering approach demonstrates significant breakthroughs over the previously reported oxide and solid electrolyte coatings in terms of stabilizing the crystal/interfacial structure over long-term cycling and high-temperature heating. Densely packed (>3.3 g cm^{-3}) Ni-rich cathodes are very attractive for next-generation electric vehicles and smart grids, which require very long calendar life and excellent abuse tolerance. However, the microcrack nucleation, phase transition and irreversible oxygen loss as well as their coupling effects have led to severe capacity fade and safety concerns in Ni-rich cathodes. This work has provided an effective approach to overcome the above issues and shed light on how rational surface engineering at both primary and secondary particle levels can suppress the oxygen release and improve battery performance. The present findings will stimulate more research regarding the fading mechanism of layered oxide cathode materials, especially voltage fade in the case of lithium- and manganese-rich layered oxide, which offers higher energy compared with NMC-based cathodes.

Methods

oCVD process. Typically, building an artificial PEDOT skin on the NCM111 particles (MTI Corp.) was carried out in a custom-built rotary oCVD system. During oCVD, EDOT (Sigma Aldrich, preheated to 110 °C) monomer and $VOCl_3$ oxidant (Sigma Aldrich) vapours were simultaneously introduced into the reactor at flow rates of 2 ± 0.2 and 0.2–0.3 sccm (standard cubic centimetres per minute), respectively. During the oCVD process, the absolute pressure of the reactor was controlled at around 300 mTorr and the heating bath was kept at 90 °C while the rotation rate was set at 140–160 r.p.m. After oCVD, the sample was rinsed with methanol followed by drying in a vacuum oven.

Morphology characterization. The morphology of the samples was characterized by scanning electron microscopy (JEOL 7100F) and TEM (FEI F200X and JEOL 2100F). To confirm the ability of oCVD to build a PEDOT skin at both primary and secondary particle levels, a Zeiss NVision 40 focused ion beam–scanning electron microscopy dual-beam system was deployed to prepare a TEM specimen from a PEDOT-skinned cathode particle through a standard lift-out procedure. To reveal the spatial distribution of the PEDOT skin layer, an FEI Talos F200X (S) TEM equipped with a SuperX energy-dispersive X-ray spectrometer was used for HAADF imaging and elemental mapping.

Chemo-physical analysis. The chemical and physical properties of the samples were determined by Fourier-transform infrared spectroscopy (Vertex 70) and micro-Raman spectroscopy (Renishaw). The particle surface was also examined by X-ray photoelectron spectroscopy (Kratos). The PEDOT skin content was determined by thermo-gravimetric analysis (TGA7, Perkin Elmer).

Electrochemical test. For the laminate preparation of the cathodes, the active material was mixed with acetylene black and poly(vinydifluoride) (8:1:1 in weight ratio) in *N*-methyl-2-pyrrolidone. The slurry was then cast onto Al foil and dried in a vacuum oven at 80 °C overnight. Type-2025 coin cells were assembled to test their electrochemical performance with Li metal as the anode, a Celgard-2025 separator and 1 M $LiPF_6$ in ethylene carbonate:ethyl methyl carbonate (EC:EMC; 3:7 by volume) as the electrolyte. Cell assembly was performed inside a glovebox (BRAUN Labstar) filled with argon gas, where the moisture and oxygen content were controlled below 0.5 ppm. The cells were cycled between 3.0 and 4.6 V at *C*/10 (1 *C* = 200 mA g^{-1}) during the initial formation process. They were charged

and discharged between 3.0 and 4.6 V at room temperature of 25 °C for the cycling stability test. The electrochemical impedance spectroscopy tests were performed on an Autolab (PGSTAT100) electrochemical station using a 5 mV a.c. perturbation with frequency ranging from 1 MHz to 0.01 Hz. Graphite laminate for the full-cell test was prepared by mixing graphite (Superior Graphite SLC1520P), conductive carbon (C45) and poly(vinydifluoride) with a weight ratio of 8:1:1. The 60-PEDOT@NCM111–graphite full cell was assembled with a negative/positive capacity ratio of around 1.1 and with 1 M $LiPF_6$ in EC:EMC (3:7 by volume) as electrolyte. It was then charged–discharged in the range of 3.0–4.5 V at *C*/10.

Thermal stability test. To harvest the charged cathode materials, coin cells with bare and PEDOT-skinned (60 min oCVD) NCM111 cathode materials were charged to 4.6 V at *C*/10 and then maintained at 4.6 V for 20 h. Before being scratched off the current collector, the charged electrodes were rinsed with dimethyl carbonate solution several times to remove the residual electrolyte. For the online gas measurement of the pure cathode by DSC–thermo-gravimetric analysis, 3.0 mg of charged electrode powder was placed in a hermetic aluminium pan, and a pinhole was punctured with a needle ion on the top centre of the pan just before the measurement to release the pressure. Before the DSC–thermo-gravimetric measurement, 3 µl electrolyte (1 M $LiPF_6$ in EC:EMC, 3:7 by volume) was added to the pan, and a pinhole was again punctured in the pan. The DSC–thermo-gravimetric measurement was conducted with a NETZSCH 449F5 simultaneous thermal analyser coupled with a NETZSCH QMS403D mass spectrometer. The temperature was increased from the ambient value of 25 to 400 °C at a ramp rate of 10 °C min^{-1}.

In situ HEXRD measurement. In situ HEXRD of bare and PEDOT-skinned NCM111 (60 min oCVD) electrodes during charge–discharge was analysed at beamline 11-ID-C of the Advanced Photon Source at Argonne National Laboratory. The wavelength was 0.117418 Å. Coin cells with holes for the beam to pass were used. The holes at the top and bottom housing of the coin cell were sealed with Kapton tape after cell assembly. During the in situ experiment, a MACCOR cycler was used to charge–discharge the cell using a constant rate of *C*/10 or 1 *C* between 2.8 and 4.6 V. The time interval between consecutive HEXRD patterns was around 10 min, which can capture all of the structural evolution during charge–discharge. The two-dimensional diffraction patterns were calibrated using a standard CeO_2 sample and converted to one-dimensional patterns using Fit2D software. For the obtained HEXRD data, the General Structure Analysis System (GSAS) software was employed to fit the observed diffraction patterns and obtain the lattice parameters. Voltage profiles are well correlated with the evolution of the HEXRD patterns. A contour plot is used to reflect the variation of the diffraction intensity, with the red and blue colours representing high and low values, respectively.

HF concentration measurement. The HF-containing electrolyte was prepared by adding H_2O to the working electrolyte following an established method[39]. Specifically, 1,000 ppm of H_2O was added to the electrolyte for 4 days of chemical reaction in the glovebox, forming the HF-containing electrolyte.

To test the PEDOT scavenging effect on HF, 20 mg of PEDOT-skinned NCM111 (60-PEDOT@NCM111) and bare NCM111 was mixed with 0.1 ml of HF-containing electrolyte for 48 h in the glovebox. Afterwards, the electrolyte was filtered and the acidity was determined by acid–base titration based on the reaction ($HF + NaOH \rightarrow NaF + H_2O$), using bromothymol blue (0.04 wt% in water) as the indicator. The solution is yellow at pH < 6 and blue at pH > 7. The titration was carried out with a 5 ml glass burette and 0.05 ml electrolyte using a 0.02 M sodium hydroxide (NaOH) aqueous solution. The titration was carried out by first placing about 3 ml of crushed ice (pH neutral) in a plastic Erlenmeyer flask with about 1 ml of pH-neutral water and a couple of drops of indicator. Then, 0.1 ml electrolyte was added to the ice slurry inside the plastic Erlenmeyer flask, where the NaOH solution was carefully metered by the burette. The addition of NaOH solution was stopped immediately when the colour of the solution turned blue (from yellow). When the blue colour lasted for 30 s, the NaOH solution amount was taken as the final acid–base titration reading. Note that the colour will eventually return to yellow, so the titration process should be performed rapidly. To rule out experimental error, each sample was titrated twice, with the result of HF given in ppm by weight of HF in the electrolyte.

Inductively coupled plasma measurement. For metal dissolution during cycling, post-test (200 cycles) coin cells were disassembled and rinsed several times with blank electrolyte (3:7 by volume of EC:EMC) in the glovebox. The organic solution was collected for HNO_3 acid digestion following an established method[40]. The digested solution was diluted to 10 ml for the inductively coupled plasma measurement. As the electrolyte volume in a coin cell cannot be determined, the metal concentrations in the 10 ml solution are presented.

Data availability

The data that support the plots within this paper and other findings of this study are available from the corresponding author on reasonable request.

Received: 7 August 2018; Accepted: 4 April 2019;
Published online: 13 May 2019

References

1. Sun, Y. K. et al. High-energy cathode material for long-life and safe lithium batteries. *Nat. Mater.* **8**, 320–324 (2009).
2. Lu, J., Wu, T. P. & Amine, K. State-of-the-art characterization techniques for advanced lithium-ion batteries. *Nat. Energy* **2**, 17011 (2017).
3. Ryu, H.-H., Park, K.-J., Yoon, C. S. & Sun, Y. K Capacity fading of Ni-rich $Li[Ni_xCo_yMn_{1-x-y}]O_2$ ($0.6 \leq x \leq 0.95$) cathodes for high-energy-density lithium-ion batteries: bulk or surface degradation? *Chem. Mater.* **30**, 1155–1163 (2018).
4. Yan, P. F., Zheng, J. M., Zhang, J. -G. & Wang, C. M. Atomic resolution structural and chemical imaging revealing the sequential migration of Ni, Co, and Mn upon the battery cycling of layered cathode. *Nano Lett.* **17**, 3946–3951 (2017).
5. Sun, Y. K. et al. Nanostructured high-energy cathode materials for advanced lithium batteries. *Nat. Mater.* **11**, 942–947 (2012).
6. Lu, J. et al. The role of nanotechnology in the development of battery materials for electric vehicles. *Nat. Nanotechnol.* **11**, 1031–1038 (2016).
7. Lu, J. et al. Effectively suppressing dissolution of manganese from spinel lithium manganate via a nanoscale surface-doping approach. *Nat. Commun.* **5**, 6693 (2014).
8. Liu, Q. et al. Approaching the capacity limit of lithium cobalt oxide in lithium ion batteries via lanthanum and aluminium doping. *Nat. Energy* **3**, 936–943 (2018).
9. Kim, U. H. et al. Pushing the limit of layered transition metal oxide cathodes for high-energy density rechargeable Li ion batteries. *Energy Environ. Sci.* **11**, 1271–1279 (2018).
10. Jung, S. K. et al. Understanding the degradation mechanisms of $LiNi_{0.5}Co_{0.2}Mn_{0.3}O_2$ cathode material in lithium ion batteries. *Adv. Energy Mater.* **4**, 1300787 (2014).
11. Lin, F. et al. Surface reconstruction and chemical evolution of stoichiometric layered cathode materials for lithium-ion batteries. *Nat. Commun.* **5**, 3529 (2014).
12. Liu, H. et al. Intergranular cracking as a major cause of long-term capacity fading of layered cathodes. *Nano Lett.* **17**, 3452–3457 (2017).
13. Kim, J. et al. A highly stabilized nickel-rich cathode material by nanoscale epitaxy control for high-energy lithium-ion batteries. *Energy Environ. Sci.* **11**, 1449–1459 (2018).
14. Yan, P. F. et al. Intragranular cracking as a critical barrier for high-voltage usage of layer-structured cathode for lithium-ion batteries. *Nat. Commun.* **8**, 14101 (2017).
15. Kim, J. et al. Prospect and reality of Ni-rich cathode for commercialization. *Adv. Energy Mater.* **8**, 1702028 (2018).
16. Zhan, C., Wu, T. P., Lu, J. & Amine, K. Dissolution, migration, and deposition of transition metal ions in Li-ion batteries exemplified by Mn-based cathodes—a critical review. *Energy Environ. Sci.* **11**, 243–257 (2018).
17. Chen, Z., Qin, Y., Amine, K. & Sun, Y. K. Role of surface coating on cathode materials for lithium-ion batteries. *J. Mater. Chem.* **20**, 7606–7612 (2010).
18. Miller, D. J., Proff, C., Wen, J., Abraham, D. P. & Bareño, J. Observation of microstructural evolution in Li battery cathode oxide particles by in situ electron microscopy. *Adv. Energy Mater.* **3**, 1098–1103 (2013).
19. Lu, J. et al. A nanostructured cathode architecture for low charge overpotential in lithium-oxygen batteries. *Nat. Commun.* **4**, 3383 (2013).
20. Li, X. et al. Atomic layer deposition of solid-state electrolyte coated cathode materials with superior high-voltage cycling behavior for lithium ion battery application. *Energy Environ. Sci.* **7**, 768–778 (2014).
21. Mohanty, D. et al. Modification of Ni-rich FCG NMC and NCA cathodes by atomic layer deposition: preventing surface phase transitions for high-voltagelithium-ion batteries. *Sci. Rep.* **6**, 26532 (2016).
22. Martha, S. K. et al. Solid electrolyte coated high voltage layered-layered lithium-rich composite cathode: $L_{i1.2}M_{n0.52}5N_{i0.17}5C_{o0.1}O2$. *J. Mater. Chem. A* **1**, 5587–5595 (2013).
23. Han, X. et al. Negating interfacial impedance in garnet-based solid-state Li metal batteries. *Nat. Mater.* **16**, 572 (2016).
24. Yan, P. F. et al. Tailoring grain boundary structures and chemistry of Ni-rich layered cathodes for enhanced cycle stability of lithium-ion batteries. *Nat. Energy* **3**, 600–605 (2018).
25. Im, S. G. & Gleason, K. K. Systematic control of the electrical conductivity of poly (3, 4-ethylenedioxythiophene) via oxidative chemical vapor deposition. *Macromolecules* **40**, 6552–6556 (2007).
26. Tenhaeff, W. E. & Gleason, K. K. Initiated and oxidative chemical vapor deposition of polymeric thin films: iCVD and oCVD. *Adv. Funct. Mater.* **18**, 979–992 (2008).
27. Malti, A. et al. An organic mixed ion–electron conductor for power electronics. *Adv. Sci.* **3**, 1500305 (2016).
28. Lee, E. J. et al. Development of microstrain in aged lithium transition metal oxides. *Nano Lett.* **14**, 4873–4880 (2014).

29. Wang, Q. et al. Origin of structural evolution in capacity degradation for overcharged NMC622 via operando coupled investigation. *ACS Appl. Mater. Interfaces* **9**, 24731–24742 (2017).
30. Liu, W. et al. Nickel-rich layered lithium transition-metal oxide for high-energy lithium-ion batteries. *Angew. Chem. Int. Ed.* **54**, 4440–4457 (2015).
31. Zhan, C. et al. Mn(II) deposition on anodes and its effects on capacity fade in spinel lithium manganate-carbon systems. *Nat. Commun.* **4**, 2437 (2013).
32. Lee, S., Paine, D. C. & Gleason, K. K. Heavily doped poly(3,4-ethylenedioxythiophene) thin films with high carrier mobility deposited using oxidative CVD: conductivity stability and carrier transport. *Adv. Funct. Mater.* **24**, 7187–7196 (2014).
33. Massonnet, N., Carella, A., Geyer, A. D., Faure-Vincent, J. & Simonata, J.-P. Metallic behaviour of acid doped highly conductive polymers. *Chem. Sci.* **6**, 412–417 (2015).
34. Zheng, J. et al. Tuning of thermal stability in layered $Li(Ni_xMn_yCo_z)O_2$. *J. Am. Chem. Soc.* **138**, 13326–13334 (2016).
35. Bak, S.-M. et al. Correlating structural changes and gas evolution during the thermal decomposition of charged $Li_xNi_{0.8}Co_{0.15}Al_{0.05}O_2$ cathode materials. *Chem. Mater.* **25**, 337–351 (2013).
36. Yan, P. F. et al. Coupling of electrochemically triggered thermal and mechanical effects to aggravate failure in a layered cathode. *Nat. Commun.* **9**, 2437 (2018).
37. Chen, Z. et al. Study of thermal decomposition of $Li_{1-x}(Ni_{1/3}Mn_{1/3}Co_{1/3})_{0.9}O_2$ using in-situ high-energy X-ray diffraction. *Adv. Energy Mater.* **3**, 729–736 (2013).
38. Liu, X. et al. Thermal runaway of lithium-ion batteries without internal short circuit. *Joule* **2**, 1–18 (2018).
39. Chen, Z. et al. New class of nonaqueous electrolytes for long-life and safe lithium-ion batteries. *Nat. Commun.* **4**, 1513 (2013).
40. Zheng, H., Sun, Q., Liu, G., Song, X. & Battaglia, V. S. Correlation between dissolution behavior and electrochemical cycling performance for $LiNi_{1/3}Co_{1/3}Mn_{1/3}O_2$-based cells. *J. Power Sources* **207**, 134–140 (2012).

Acknowledgements

Research at the Argonne National Laboratory was funded by the US Department of Energy, Vehicle Technologies Office. Use of the Advanced Photon Source and the Centre for Nanoscale Materials, both Office of Science user facilities, was supported by the US Department of Energy, Office of Science and Office of Basic Energy Sciences, under contract no. DE-AC02-06CH11357. Research in Hong Kong was funded by the Hong Kong Research Grant Council (PolyU163208/16P), a postgraduate studentship from HKUST and the area of Excellence fund of HKPolyU (1-ZE30). G.-L.X., Z.C. and K.A. gratefully acknowledge support fromt the US department of Energy, Office of Energy Efficiency and Renewable Energy, Vehicle Technologies Office. K.A., F.P. and M.O. also thank Clean Vehicles, US–China Clean Energy Research Centre (CERC-CVC2), for support.

Author contributions

K.A., G.C. and G.-L.X. initiated this research project. Q.L. carried out oCVD with help from K.K.S.L. and performed the half-cell performance test with the help of J.L. and M.S. G.-L.X. performed the full-cell performance test. Q.L. and G.-L.X. performed morphology and physical structure analysis. G.-L.X., H.G., M.Z., F.P., Z.C. and Y.R. conducted in situ HEXRD measurement and analysis. G.-L.X., X.Z. and Y.L. conducted focused ion beam TEM characterization and analysis. X.L. and M.O. performed thermal stability and oxygen evolution characterization on charged cathodes. G.-L.X., Q.L., K.A. and G.C. prepared the manuscript with input from all authors.

Competing interests

The authors declare no competing interests.

Additional information

Supplementary information is available for this paper at https://doi.org/10.1038/s41560-019-0387-1.

Reprints and permissions information is available at www.nature.com/reprints.

Correspondence and requests for materials should be addressed to K.A. or G.C.

Publisher's note: Springer Nature remains neutral with regard to jurisdictional claims in published maps and institutional affiliations.